



HAL
open science

Performance optimization of ZnO nanowire/parylene-C composite-based piezoelectric nanogenerators

Manuel Manrique, Vincent Consonni, Gustavo Ardila, Aymen Ghouma,
Gwenaël Le Rhun, Bassem Salem

► **To cite this version:**

Manuel Manrique, Vincent Consonni, Gustavo Ardila, Aymen Ghouma, Gwenaël Le Rhun, et al..
Performance optimization of ZnO nanowire/parylene-C composite-based piezoelectric nanogenerators.
Nano Trends, 2025, 9, pp.100066. 10.1016/j.nwnano.2024.100066 . hal-04839530

HAL Id: hal-04839530

<https://hal.science/hal-04839530v1>

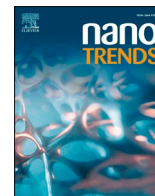
Submitted on 16 Dec 2024

HAL is a multi-disciplinary open access archive for the deposit and dissemination of scientific research documents, whether they are published or not. The documents may come from teaching and research institutions in France or abroad, or from public or private research centers.




L'archive ouverte pluridisciplinaire **HAL**, est destinée au dépôt et à la diffusion de documents scientifiques de niveau recherche, publiés ou non, émanant des établissements d'enseignement et de recherche français ou étrangers, des laboratoires publics ou privés.



Distributed under a Creative Commons Attribution 4.0 International License



Performance optimization of ZnO nanowire/parylene-C composite-based piezoelectric nanogenerators

Manuel Manrique^{a,b,c} , Vincent Consonni^{b,*} , Gustavo Ardila^d , Aymen Ghouma^a ,
Gwenaël Le Rhun^c , Bassem Salem^{a,*} 

^a Univ. Grenoble Alpes, CNRS, CEA/LETI Minatec, Grenoble INP, LTM, F-38054, Grenoble, France

^b Univ. Grenoble Alpes, CNRS, Grenoble INP, LMGP, F-38000, Grenoble, France

^c Univ. Grenoble Alpes, CEA, LETI, F-38000, Grenoble, France

^d Univ. Grenoble Alpes, Univ. Savoie Mont Blanc, CNRS, Grenoble INP, CROMA, F-38000, Grenoble, France

ARTICLE INFO

Keywords:

Piezoelectric nanogenerators
ZnO nanowires
Chemical bath deposition
Parylene-C

ABSTRACT

Piezoelectric nanogenerators (PNGs) based on ZnO nanowires embedded in a polymer matrix have shown great promise in converting ambient mechanical energy into electrical energy, positioning them as candidates for autonomous sensor applications. Here, we fabricate vertically integrated ZnO NW/parylene-C composite-based PNGs using a capacitive configuration. By carefully controlling the thickness of the parylene-C top layer over ZnO nanowire arrays, four PNGs with parylene-C top layer thicknesses ranging from 1.1 to 3.2 μm were successfully fabricated. Raman spectroscopy suggests that the parylene-C does not affect the crystallographic properties of ZnO nanowires when coated. In addition, electrical impedance measurements reveal that increasing the parylene-C top layer thickness decreases the PNG capacitance, leading to higher internal impedance. The performance of these PNGs is assessed through piezoelectric characterizations across a range of load resistances, from 50 k Ω to 122 M Ω , under vertical compression forces of 1 N applied at 0.2 Hz. These tests have identified an optimal parylene-C top layer thickness of around 2 μm , resulting in an instantaneous power density of 1.8 $\mu\text{W}/\text{cm}^3$ generated by the PNG. These findings highlight promising pathways for enhancing the efficiency and performance of PNGs.

1. Introduction

The development of Internet of Things (IoT) since the 1970s has revolutionized various industrial sectors, including healthcare, agriculture, and daily life, by connecting physical objects to digital technologies [1,2]. This has increased the need for Wireless Sensor Networks (WSNs), which require efficient and sustainable power sources [3], such as energy harvesters converting renewable energy from the environment into electricity. The piezoelectric nanogenerators (PNGs), as electronic devices converting ambient mechanical energy into electrical energy, have emerged as promising power suppliers for developing autonomous smart systems, although their low energy conversion efficiency remains a challenge [3,4]. Recent advances in nanotechnology, particularly involving piezoelectric nanowires (NWs), have significantly boosted the efficiency of PNGs [5]. Among the piezoelectric materials synthesized as NWs, zinc oxide (ZnO), known for its abundance and biocompatibility, has widely been used in PNGs since its first application in 2006 [6].

Nowadays, the PNG consisting of a ZnO NW/polymer composite vertically integrated between two metallic electrodes according to the capacitive configuration is the most commonly developed architecture, owing to its relatively easier manufacturing and effectiveness in harvesting compressive and bending mechanical energy [7,8]. In this PNG architecture, the polymer mainly serves three crucial functionalities: i) it provides mechanical robustness to the device, ii) it enables a capacitive contact between the ZnO NWs and top metallic electrode, preventing leakage current or short circuits due to the semiconducting properties of n-doped ZnO NWs, and iii) it can enhance the electro-mechanical coupling properties of the device, improving its energy conversion efficiency [9]. In addition, the polymer isolates ZnO NWs from their neighbors, preventing a direct contact during mechanical deformation of the PNG. This electrical isolation could prevent detrimental screening effects involving free electron tunneling phenomena between neighboring ZnO NWs, which reduces the PNG performance [10,11]. The most commonly used polymers in ZnO NW-based PNGs include poly

* Corresponding author.

E-mail addresses: vincent.consonni@grenoble-inp.fr (V. Consonni), bassem.salem@cea.fr (B. Salem).

<https://doi.org/10.1016/j.nwnano.2024.100066>

Received 6 November 2024; Received in revised form 2 December 2024; Accepted 4 December 2024

Available online 5 December 2024

2666-9781/© 2024 The Author(s). Published by Elsevier Ltd. This is an open access article under the CC BY-NC license (<http://creativecommons.org/licenses/by-nc/4.0/>).

(methyl methacrylate) (PMMA) [12,13], poly(dimethylsiloxane) (PDMS) [14], and parylene-C [15,16]. Notably, recent alternatives, such as polycarbonate [17], S1818 [18], and SU-8 [19], have also been explored. These polymers, with their lower Young's modulus and relative dielectric permittivity than ZnO NWs, improve the PNG performance [20]. Hinchet et al. demonstrated *via* finite element method (FEM) simulations that reducing the thickness of the top polymer layer enhances mechanical energy transfer to the ZnO NW matrix, in turn boosting the PNG performance [9]. These simulations are consistent with experimental results from ZnO NW/PMMA composite-based PNGs, which confirm that reducing the thickness of the top polymer layer improves the PNG performance. However, the experimental data also reveals that excessively thin top polymer layers cause performance loss due to leakage currents [13,21]. Consequently, an optimal PMMA top layer thickness lying in the range of 1.2 to 1.5 μm was identified as maximizing the performance of ZnO NW-based PNGs. For ZnO NW/PDMS composite-based PNGs, the polymer top layer thickness can vary from 7 μm to 200 μm [14,22]. Although both PMMA and PDMS have favorable properties for piezoelectric applications, including low Young's modulus and relative dielectric permittivity [20], they are deposited *via* spin-coating, which is a method with significant limitations, involving challenges in achieving conformal polymer infiltration into the ZnO NW matrix, a low process reliability, and time-consuming. In contrast, parylene-C ($\text{C}_{16}\text{H}_{14}\text{Cl}_2$), as a polymer with a Young's modulus [23] between 2.4 and 4 GPa and a relative dielectric permittivity [24] in the range of 2.7 and 6.1, has arisen as a promising alternative to replace PMMA and PDMS. ZnO NW/parylene-C composite-based PNGs, was first developed by Dahiya A.S. et al, in 2018 [15], these PNGs have generated power densities up to 4 mW/cm^2 [25], surpassing the power densities of PNGs based on ZnO NW/PMMA and ZnO NW/PDMS composites [14,26]. In addition, parylene-C is deposited through vacuum evaporation and polymerization processes, enabling consistent infiltration into the ZnO NW matrix and precise control of the top layer thickness. However, unlike PMMA and PDMS, the effect of the thickness of the parylene-C top layer on PNG performance has not been properly investigated yet. Studies have shown that reducing the thickness of the polymer top layer enhances the output voltage of PNGs. However, thinner layers can introduce leakage currents, which in turn degrade the output voltage. This observation suggests the existence of an optimal thickness for the top layer.

To address this issue, the present investigation focuses on optimizing the thickness of the parylene-C top layer in a PNG based on ZnO NWs grown by chemical bath deposition (CBD), a green chemistry compatible process that allows the synthesis of ZnO NWs at temperatures ranging from 60 to 90 $^{\circ}\text{C}$. Four distinct PNGs based on ZnO NW/parylene-C composites are fabricated, each of them with varying parylene-C top layer thickness. The morphology of the synthesized ZnO NWs and the conformal deposition of the parylene-C layer are analyzed *via* field-emission scanning electron microscopy (FESEM) imaging and FESEM-Energy Dispersive X-ray Spectroscopy (EDS) mapping. Raman spectroscopy is performed to assess the structural properties of ZnO NWs coated with parylene-C. Finally, the internal impedance and

piezoelectric properties of the PNGs are evaluated through electrical and electromechanical measurements, revealing the optimal thickness of parylene-C top layer for boosting the PNG performance.

2. Experimental section

2.1. Fabrication of piezoelectric nanogenerators based on ZnO nanowires/parylene-C composites

PNGs were fabricated on n-type highly doped (100) Si substrates (0.001–0.004 Ωcm), as detailed in Fig. 1. First, polycrystalline ZnO seed layers were grown by sol-gel process on pre-cleaned (100) Si substrates (1). A solution mixing zinc acetate dehydrate ($\text{Zn}(\text{CH}_3\text{COO})_2 \cdot 2\text{H}_2\text{O}$, Sigma-Aldrich) and monoethanolamine (MEA, Sigma-Aldrich) in equimolar concentration of 375 mM in pure ethanol was prepared and stirred for 12 h at 60 $^{\circ}\text{C}$ and then 12 h at room temperature. The (100) Si substrates, pre-cleaned in an ultrasonic bath with acetone and isopropyl alcohol, were subsequently dipped into the solution under a controlled atmosphere (<16 % hygrometry) and finally annealed at 300 $^{\circ}\text{C}$ for 10 min on a hot plate and at 500 $^{\circ}\text{C}$ for 1 h in a regular oven. Second, ZnO NWs were grown on the polycrystalline ZnO seed layer-coated Si substrates (2). The latter were placed face down in sealed reactors containing a 54 ml aqueous solution consisting of zinc nitrate hexahydrate ($\text{Zn}(\text{NO}_3)_2 \cdot 6\text{H}_2\text{O}$, Sigma Aldrich) and hexamethylenetetramine (HMTA, Sigma Aldrich) with an equimolar concentration ratio of 50 mM. The initial pH of the chemical bath (pH_0) was fixed at ~ 10.6 by adding ~ 600 mM of ammonia (NH_3 , Sigma Aldrich). The growth of ZnO NWs was achieved by keeping the sealed reactors in a regular oven heated at 85 $^{\circ}\text{C}$ for 3 h. Third, the ZnO NWs were encapsulated by parylene-C layers deposited by vacuum deposition according to the Gorham method (3) [27]. The thickness of parylene-C layers was controlled by different dimmer masses of GALAXYL* C, which followed a i) sublimation at around 120 $^{\circ}\text{C}$, ii) pyrolysis at 690 $^{\circ}\text{C}$ splitting the dimer into monomers, and iii) condensation and polymerization processes of the gaseous monomer in the surface of the substrates at room temperature. Forth, the $1 \times 1\text{cm}^2$ top electrode assisted by a mask was obtained by the stack of 3 metallic layers: 20 nm-thick of Ti layer, 250 nm-thick of Al layer and 100 nm-thick of Au layer using e-beam evaporator (4). Finally, both the bottom (Si substrate) and top electrodes were contacted by two Cu wires using a conductive resin (5).

2.1.1. Characterization techniques

The structural morphology properties of ZnO NWs were assessed with a FEI Quanta 250 field-emission scanning electron microscopy (FESEM) instrument.

FESEM-EDS spectra were recorded on ZnO NWs and PNGs using a Bruker X-ray detector incorporated in the FEI Quanta 250 FESEM instrument operating at 15 kV.

The Raman scattering at room temperature was performed using a Horiba/Jobin Yvon Labram spectrometer equipped with a liquid nitrogen-cooled CCD detector. A 514.5 nm excitation line of an Ar^+ laser with a power on the sample surface of 0.8 mW was focused on a spot size

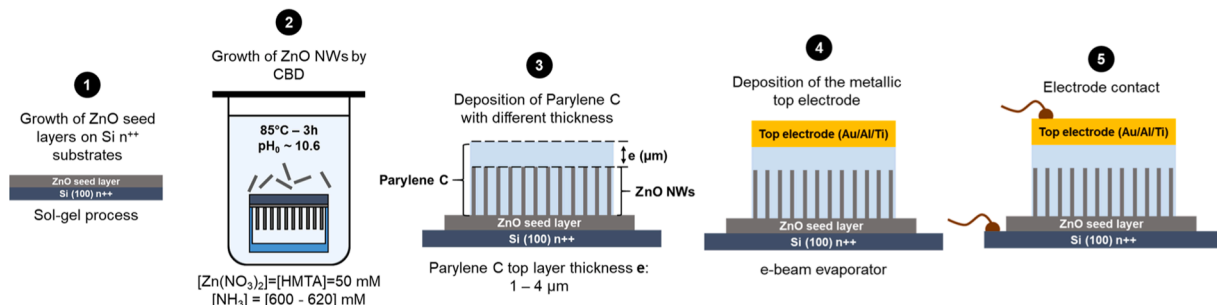


Fig. 1. Fabrication steps of PNGs with distinct parylene-C top layer thicknesses.

of $1 \mu\text{m}^2$ using a $50\times$ objective. A Si reference sample was used for the spectral calibration in wavenumber using the theoretical Raman line set to 520.7 cm^{-1} .

The internal impedance of PNGs was measured with a Keysight E4980A/AL LCR meter controlled by a Python program. An AC voltage of 1 Vpp along with a bias of 1 V were applied between the bottom and top electrodes of the PNG over a frequency band from 20 to 495 Hz.

The automated test bench for piezoelectric characterizations of PNGs included an actuator, sample holder, force load, and force sensor, as detailed in REF [21]. The z -position of the sample holder was regulated with an LAL35-025-62F (SMAC Carlsbad California) linear magnetic actuator monitored by a LabVIEW-based software from the PC unit. The PNG was placed on the sample holder, which was manually adjusted in the x - and y -directions. A force sensor connected to a force load was

positioned above the PNG. The force load, consisted of a metallic cylinder affixed to a plastic screw, was designed to prevent triboelectric-related effects during piezoelectric characterizations. A vertical force was applied by the metallic cylinder on the top electrode of the PNG as the actuator moved in the z -direction. The force magnitude was managed via PC unit using LabVIEW-based software. The PNG electrodes were connected in parallel to an external load ranging from 50 k Ω to 122 M Ω , with a preamplifier used to measure the voltage drop across the external load. This voltage drop was recorded using a Tektronix MSO44 4 Series oscilloscope.

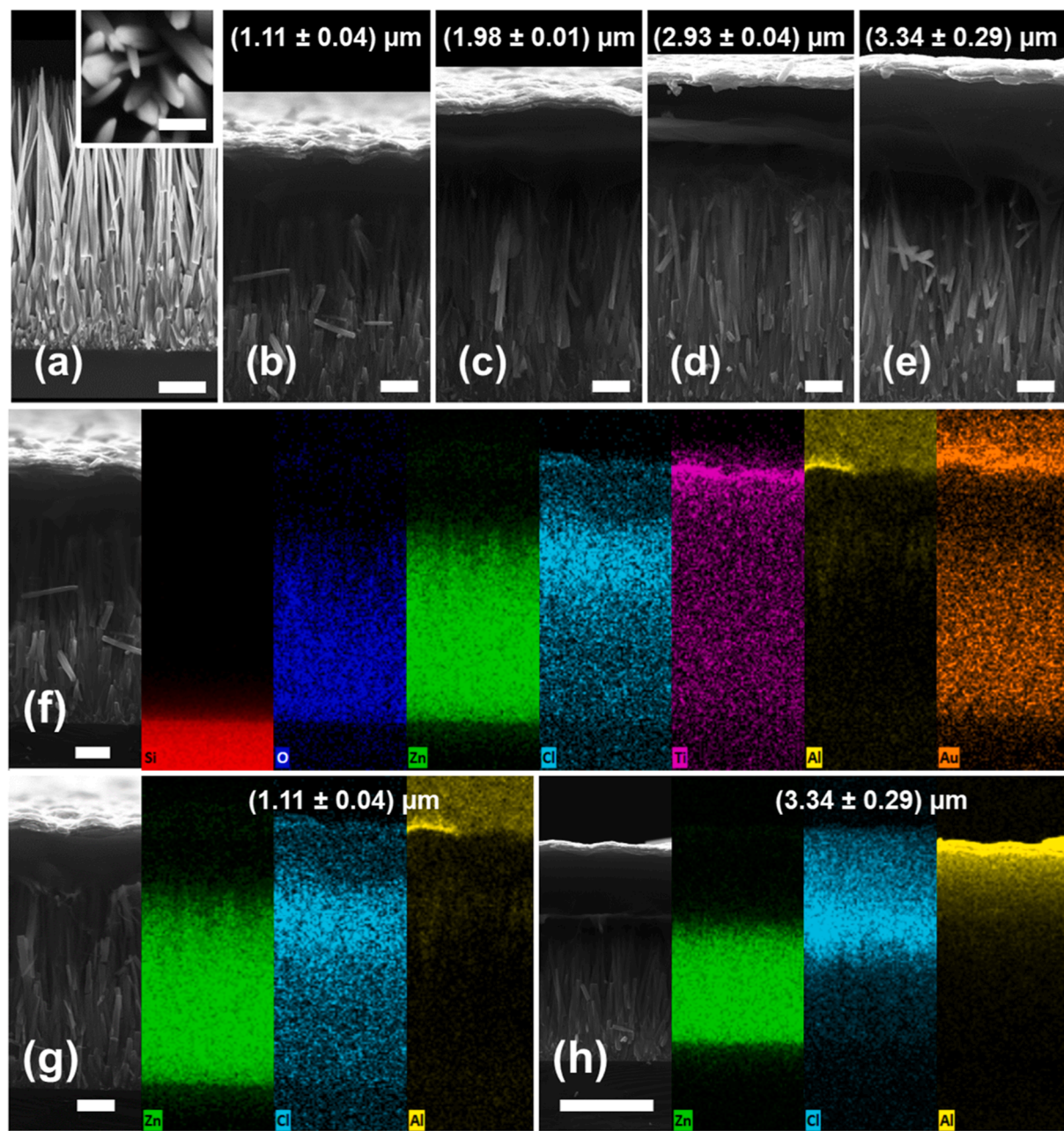


Fig. 2. FESEM images of the (a) cross-section and (inset) top view of the grown ZnO NWs, and (b–e) the cross-section of the four fabricated PNGs with different thicknesses of the parylene-C top layer. (f) FESEM-EDS mapping of a PNG's cross-section displaying the bottom electrode (Si-red), ZnO NW matrix (O-blue and Zn-green), parylene-C layer (Cl-blue-sky), and the top electrode (Ti-purple, Al-yellow and Au-orange). FESEM-EDS mapping of the PNG's cross-section with (g) 1.11 and (h) 3.34 μm -thick parylene-C top layer. The bar scale corresponds to 1 μm , except for the inset of (a) which corresponds to 200 nm.

3. Results and discussion

3.1. Structural morphology of ZnO NW/parylene-C composites

The homoepitaxial and heterogeneous growth of vertically aligned ZnO NWs was achieved on polycrystalline ZnO seed layers oriented along the polar *c*-axis [28]. These ZnO NWs grown by CBD in a high pH-region exhibit hexagonal sections, which are characteristic of their wurtzite structure, as revealed in Fig. 2(a) by FESEM images. The diameter of ZnO NWs progressively decreases from their bottom to their top, resulting in a pencil-like shape, due to a faster axial growth rate along the polar *c*-axis compared to the radial growth rate along the non-polar *m*-axis [29]. The mean diameters are (42 ± 21) nm at the top and (166 ± 40) nm at the middle of the NW height, with a mean length of (5.5 ± 0.4) μm . This gives an aspect ratio (defined as the mean length over the mean diameter) of 33.1 ± 8.3 . The number density of ZnO NWs is typically (43.3 ± 8.2) $\text{NW}/\mu\text{m}^2$. In addition, the cross-sectional FESEM images of the PNGs (Fig. 2(b–e)) reveal the presence of parylene-C top layer over the ZnO NW arrays. This shows the successful fabrication of four PNGs with parylene-C top layers exhibiting a given thickness varying in the range of 1.11 to 3.34 μm .

To ensure the mechanical stability and proper electrical isolation between ZnO NWs, the infiltration of parylene-C into the NW matrix was evaluated using cross-sectional FESEM-EDS mapping, as shown for the PNG with a 1.11 μm -thick parylene-C top layer in Fig. 2(f). In these elemental maps, the different components of the PNG are color-coded. The ZnO NWs (blue and green regions for O and Zn, respectively) are vertically integrated on the bottom electrode (red region for Si substrate) and coated by the parylene-C layer (blue-sky region for Cl). This polymer successfully infiltrates the NW arrays, ensuring their effective mechanical robustness and electrical isolation. Parylene-C also establishes capacitive coupling between the ZnO NWs and top metallic electrode of the PNG, preventing leakage currents. Regarding the top metallic electrode of the PNG, the deposition of the Ti layer appears to induce a diffusion process of Ti atoms across the device, as suggested by the dispersed purple region. In contrast, the Ti layer prevents the diffusion process of Al atoms into the device, as shown by the localized yellow region. The Au layer (orange region) is well confined over the Al layer on the top electrode, although traces of Au were detected in the composite matrix. This apparent Au presence could be due to the cleavage required for collecting cross-sectional FESEM images.

Moreover, cross-sectional FESEM-EDS maps of the PNGs with parylene-C top layer thicknesses of 1.11 and 3.34 μm , as shown in Fig. 2 (g, h), suggest a non-homogeneous density distribution of the parylene-C layer over the ZnO NW matrix, indicated by the denser blue-sky region at the top of the NW arrays. This non-uniformity could be related to the number density and spatial distribution of the NWs. Despite the presentment statement, the parylene-C layer thickness is well-controlled across the ZnO NW arrays, confirming the reliability of the deposition process.

3.2. Raman spectroscopy

To thoroughly investigate the potential residual mechanical stress in ZnO NWs induced by the parylene-C coating layer, Raman scattering spectroscopy was performed thanks to the strong coupling between the phonon modes of ZnO NWs and their crystallographic properties. Fig. 3 presents the Raman scattering spectra for ZnO NWs coated with a parylene-C layer (green), a parylene-C layer-coated Si substrate (yellow), ZnO NWs on a Si substrate (blue), and a reference Si substrate (dotted line). It is worth mentioning that the Raman scattering spectra were carefully recorded over a wavenumber range of 50 to 3750 cm^{-1} with a total acquisition time of 600 s (10 recordings of 60 s each) to prevent sublimation of the parylene-C layer. In addition, all the Raman scattering spectra were calibrated and normalized according to the position (520.7 cm^{-1}) and the intensity of the Si Raman line, respectively.

In the low-wavenumber region of 50–1620 cm^{-1} , the ZnO NWs with the wurtzite structure exhibit first phonon modes at 99 (E_2^{low}), 380 ($A_1(\text{TO})$), 438 (E_2^{high}) and 581 ($A_1(\text{LO})$) cm^{-1} , as well as second phonon modes at 204 ($2\text{TA}/2 E_2^{\text{low}}$) and 333 ($E_2^{\text{high}} - E_2^{\text{low}}$) cm^{-1} [30]. The pronounced shoulder observed between 1048 and 1191 cm^{-1} is assigned to phonon modes related to ZnO. The Raman lines associated with the parylene-C layer, marked by yellow stars, are mainly assigned to carbon-related bonds [31]. In the wavenumber region of 50–700 cm^{-1} , the Raman lines at 164, 243, and 689 cm^{-1} correspond to translational and rotational lattice vibrations, C–C in-plane bending, and C–Cl stretching vibrations, respectively [31,32]. In the wavenumber region of 700–1620 cm^{-1} , the Raman lines at 870 and 912 cm^{-1} are attributed to CH out-of-plane deformations; those at 1003, 1050, and 1209 cm^{-1} are assigned to CH in-plane deformations, the line at 1339 cm^{-1} corresponds to CH_2 wagging and twisting vibrations; and the lines at 1404, 1443, and 1608 cm^{-1} are attributed to CH scissoring in CH_2 and/or C–C

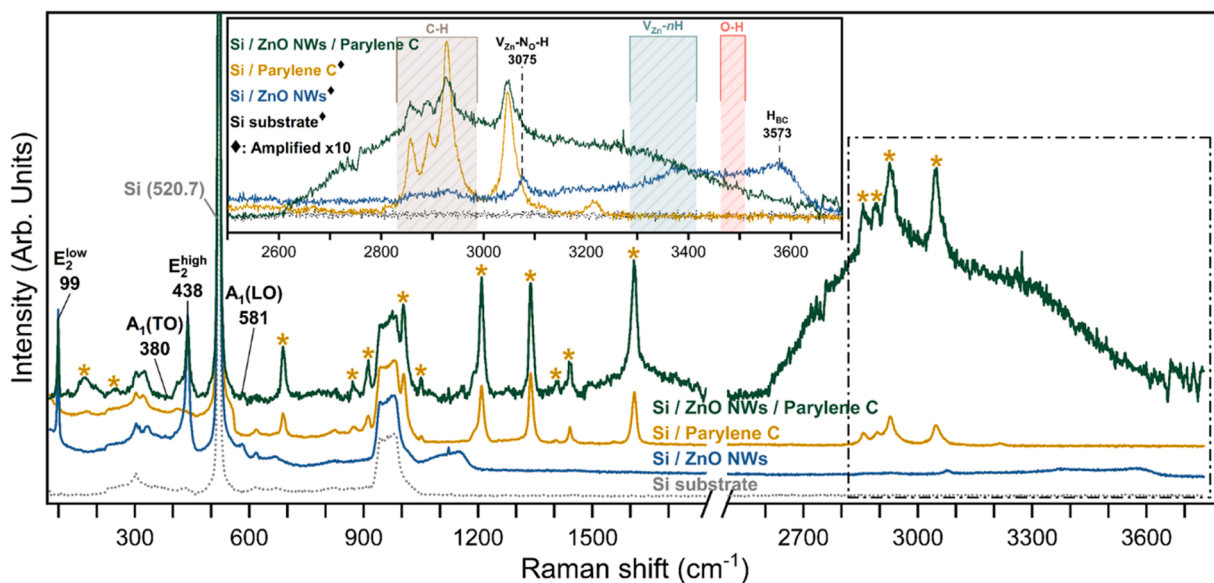


Fig. 3. Raman spectra of ZnO NWs coated with a 1.11 μm -thick parylene-C layer. Zoom-in of the high wavenumber region (inset). The spectra of reference samples were amplified by a 10-factor for the sake of clarity.

skeletal in-plane vibrations of the aromatic ring [31].

In the high-wavenumber region of 2500–3750 cm^{-1} , as zoomed in the inset of Fig. 2, the Raman lines arising from carbon-, nitrogen-, and hydrogen-related defects occur. The broad Raman band observed from 2850 to 2990 cm^{-1} (brown area) proceeds from C–H_x ($x = 1, 2, 3$) bonds, as a result of molecular carbon-adsorption processes on the m -plane sidewalls of ZnO NWs coming from HMTA molecules [33]. The weak Raman line at 3075 cm^{-1} is assigned to V_{Zn}–N_O–H complexes in ZnO NWs [34]. The broad Raman region noticed between 3100 and 3200 cm^{-1} (turquoise area) derives from V_{Zn}–xH ($x = 1, 2, 3$) defect complexes [35–37], while the asymmetric Raman shoulder observed from 3480 to 3650 cm^{-1} includes the contribution of O–H bonds (red area) [38] on the surface of ZnO NWs and H_{BC} [39] in their bulk. Regarding the parylene-C layer, four Raman lines at 2860, 2890, 2928, and 3045 cm^{-1} occur, which are related to stretching vibrations of C–H bonds from the aromatic ring [31,40].

Furthermore, the position and intensity of both the E₂^{low} and E₂^{high} Raman lines of ZnO NWs remain unchanged when coated with the parylene-C layer, as well as no additional phonon modes are observed. This suggests that the parylene-C coating layer does not alter the crystallographic properties of the ZnO NWs, hence it does not introduce any mechanical stress into the NWs [41]. Consequently, the parylene-C coating layer appears not to affect the spontaneous polarization field of ZnO NWs [42,43]. In contrast, the strong fluorescence observed in the polymer-embedded ZnO NWs at high wavenumbers could indicate a modification of the optical properties of ZnO NWs when coated with parylene-C.

3.3. Internal impedance of piezoelectric nanogenerators

The module of the internal impedance of the PNGs (Z_{PNG}) was measured over a frequency band from 20 to 495 Hz, by applying an AC voltage of 1 V_{pp} between their top and bottom electrode, and measuring the current.

The active piezoelectric component of the fabricated PNGs can be divided into three distinct layers: i) a ZnO seed layer, ii) a bottom composite layer, which consists of the ZnO NWs impregnated by the parylene-C layer, iii) and a parylene-C top layer, which refers to the parylene-C over the NWs with different thicknesses. Therefore, the equivalent electronic circuit of a PNG can be modeled as three impedances in series involving a resistance R_i in parallel with a capacitance C_i [13], as schematized in Fig. 4(a). The electrical resistance is calculated

as $R_i = \rho_b \frac{L_i}{A_i}$, where ρ_b , L_i , A_i refer to the resistivity, thickness, and active area of the studying layer, respectively. The capacitance is given by $C_i = \epsilon_0 \epsilon_i \frac{A_i}{L_i}$, where ϵ_0 and ϵ_i are the dielectric permittivity of the vacuum and of the analyzed layer, respectively. By considering the bottom composite layer as an effective homogeneous material, the mathematical expression of its impedance involves the volume fraction V of each material (i. e. ZnO NWs and the parylene-C) along with their electrical and mechanical properties, resulting in a complex mathematical expression of the bottom composite layer impedance [13]. However, given that the four manufactured PNGs differ only in the thickness of the polymer top layer, the variation in their corresponding Z_{PNG} is mainly related to the properties of this parylene-C top layer.

Fig. 4(b) presents the impedance module ($|Z_{TOTAL}| = Z_{PNG}$) of the four fabricated PNGs as a function of working frequency. The devices are labeled as PNG-A, PNG-B, PNG-C, and PNG-D according to the thickness of the parylene-C top layer of 1.11, 1.98, 2.93, and 3.34 μm , respectively. Then, increasing the thickness of the parylene-C top layer leads to an increase in Z_{PNG} , suggesting that a thicker polymer top layer leads to an increase in the electrical resistance while simultaneously reducing the capacitance of the device, resulting in higher Z_{PNG} . In addition, the frequency dependence of Z_{PNG} confirms that the devices exhibit capacitive behavior, indicating that they are not short-circuited and are available for piezoelectric characterizations. For operating frequencies below 1 Hz, the Z_{PNG} is expected to exceed 49.6, 56.6, 117.4, and 192.7 M Ω for PNG-A, PNG-B, PNG-C, and PNG-D, respectively, by fitting a linear regression in the graph $\log(|Z|) - \log(\text{Frequency})$. In theory, connecting an external resistive load in parallel with the PNGs, with values within the range of Z_{PNG} , would enable PNGs to generate a maximum power density under mechanical stress, as further discussed in the piezoelectric characterizations.

3.4. Performance of piezoelectric nanogenerators

The piezoelectric performance of the PNGs was assessed with an electromechanical setup, as shown in Fig. 5a. In this setup, the PNG was placed on a sample holder that was moved vertically (z -direction) by an actuator, compressing the PNG against a metallic cylinder of the force load. The piezoelectric characterizations were performed by applying a 1 N force vertically to the top metallic electrode of the PNG at a frequency of 0.2 Hz, as presented in Fig. 5b. During each mechanical compression and release cycle, the device generated two piezoelectric

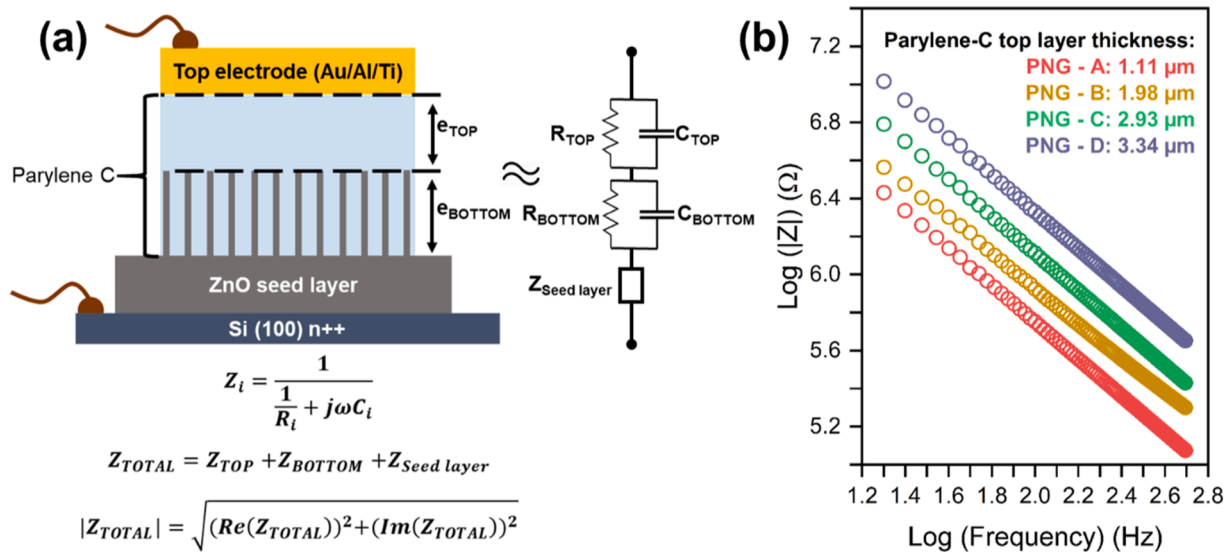


Fig. 4. (a) Equivalent electronic circuit a PNG vertically integrating a ZnO NW matrix impregnated by a parylene-C layer. (b) Measurement of internal impedances of PNG with different thicknesses of parylene-C.

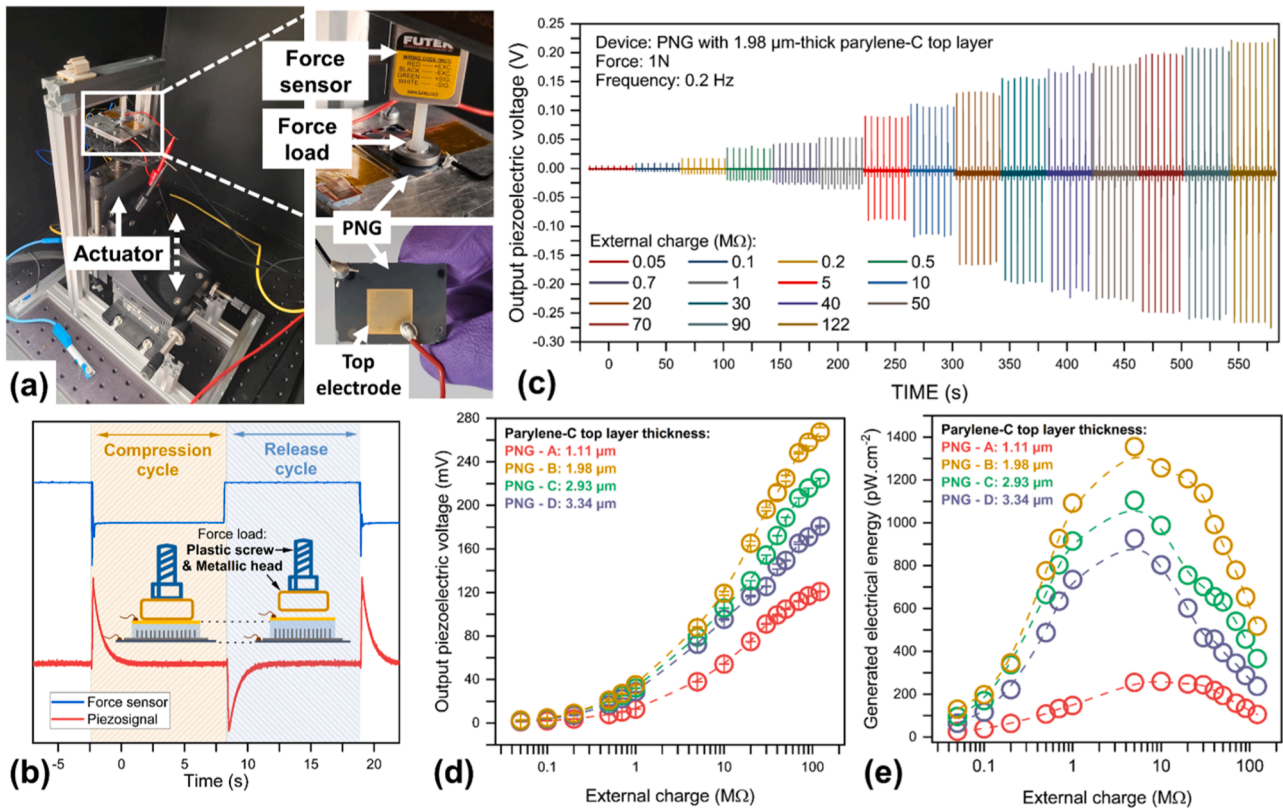


Fig. 5. (a) Photo of the electromechanical test bench for piezoelectric characterization along with the final PNG device. (b) Piezoelectric characterization of a PNG. (c) Output voltage of a PNG with 1.98 μm-thick parylene-C top layer according to the external charge connected in parallel. Comparison of the (d) output voltage and the (e) instantaneous power density between the PNGs with different thicknesses of the parylene-C top layer.

peaks of opposite polarity, measured across an external resistive load connected in parallel to the PNG. Owing to the uncontrolled impact force between the PNG and the force load at the beginning of each mechanical compression cycle, higher forces than expected are applied, resulting in positive piezoelectric peaks with variable amplitudes. Therefore, only the negative piezoelectric peaks, generated during the controlled mechanical release cycle, were used to assess the PNG performance. In addition, a reference PNG (fabricated without ZnO NWs) was characterized in the test bench, with no electrical signal detected. This strongly suggests the absence of contact electrification effects, eliminating the possibility of misinterpreting piezoelectric signals [44].

The output voltage of the PNGs with parylene-C top layer thicknesses of 1.11, 1.98, 2.93, and 3.34 μm, labeled PNG-A, PNG-B, PNG-C, and PNG-D, respectively, were investigated across external loads from 50 kΩ to 122 MΩ. As shown in Fig. 5c, the output voltage of the PNGs (PNG-B in this example) increases steadily as the resistive load rises up to 122 MΩ. This behavior can be explained through an equivalent Thevenin model, where the PNG is represented by a controllable voltage source (open-circuit voltage, V_{OC}) in series with a resistive charge (internal impedance of the PNG, Z_{PNG}) [45]. When an external load Z_L is connected in parallel to the PNG, the output voltage V_m across Z_L is given by the expression: $V_m = \frac{Z_L}{Z_L + Z_{PNG}} V_{OC}$. This equation shows that V_m increases with Z_L , approaching V_{OC} as Z_L significantly exceeds Z_{PNG} [45,46]. The output voltage peaks of the PNGs during the release mechanical cycle as a function of Z_L are summarized in Fig. 5d. The output voltages of all PNGs increase consistently as Z_L rises up to 122 MΩ, indicating that external loads exceeding 122 MΩ are needed to achieve an “open-circuit regime”, as no voltage saturation is observed. The PNG-A generates the lowest output voltages, ranging from 1.2 to 120.8 mV as Z_L increases from 50 kΩ to 122 MΩ. In contrast, the highest output voltages are generated by the PNG-B, with values rising from 2.7 to 267.4 mV over the same Z_L range. Then, the output voltage gradually decreases for the

PNG-C and PNG-D as the parylene-C top layer thickness increases.

Considering Ohm’s law, the instantaneous electrical power density generated by the PNGs can be calculated as $P = (V_m)^2 \times \frac{1}{Z_L} \times \frac{1}{A}$, where A is the active area of the PNG ($A = 1.12 \text{ cm}^2$, corresponding to the area of the metallic cylinder of the force load). Then, the variation of P as a function of Z_L is presented in Fig. 5e. The PNGs exhibit their maximum power density with Z_L between 5 and 10 MΩ, after which the power density steadily decreases as Z_L increases. As expected, the PNG-A consistently generates the lowest power density among the devices, reaching its maximum value of 259.9 pW.cm⁻² with a Z_L of 10 MΩ. In contrast, the PNG-B achieves a maximum power density of 1355.3 pW cm⁻² for a Z_L of 5 MΩ, which is 5.2 times higher than that of the PNG-A. Similarly, the PNG-C and PNG-D generate their maximum power density of 1104.3 and 926.0 pW cm⁻², respectively, with a Z_L of 10 MΩ, which are lower than that of the PNG-B.

These findings reveal that: i) the Z_L required to generate the maximum power density in the PNGs does not coincide with Z_{PNG} , and ii) it exists an optimal thickness of parylene-C that boosts the PNG efficiency.

The discrepancy between the expected and experimental load resistance for achieving the maximum power density could be due to the square waveform of the applied force. The capacitive and resistive characteristics of the Z_{PNG} could likely influence the harmonic contributions of the generated voltage under square waveform mechanical excitations, and so affecting the maximum power density [45].

Moreover, it has been shown that reducing the thickness of the polymer top layer increases the mechanical deformation of ZnO NWs under compressive stress, which in turn boosts the output voltage of the PNG [9,13]. In the present work, a 1.98 μm-thick parylene-C layer over the ZnO NWs yielded the highest PNG performance. When the parylene-C top layer is thicker than 1.98 μm, both the transfer of mechanical deformation to the ZnO NWs and the capacitance of the PNG

are reduced, resulting in decreased PNG performance [9,13,21]. Conversely, a parylene-C top layer thinner than 1.98 μm increases the risk of leakage current, which similarly compromises the PNG performance. Thus, an optimal balance between mechanical energy transfer and electrical energy storage is required, which was experimentally observed in PNGs based on ZnO NWs embedded in PMMA, PDMS, and parylene-C matrix, whose features are presented in Table 1.

Among PNGs based on flexible PET, PEN, and PDMS substrates reported in the literature, the one incorporating a parylene-C layer exhibits the best energy conversion efficiency. Similarly, PNGs based on rigid substrates (Si and Quartz) with a parylene-C layer show the highest power density, highlighting the advantages of parylene-C for vertically integrated ZnO NW-based PNGs. In addition, the deposition of parylene-C by vacuum evaporation at room temperature is both uniform and reproducible, offering a more reliable alternative to PMMA and PDMS, which require careful control of multiple parameters to achieve consistent results through the spin-coating process. The PNG-B in the present work exhibits interesting performance among the parylene-C-based PNGs. Notably, our devices were tested under relatively soft mechanical stress and working frequency, suggesting they could produce even higher output voltage and power density with forces exceeding 1 N applied at frequencies above 0.2 Hz. Another factor that could enhance the energy harvesting of our devices would be to improve the electrical conductivity of the bottom electrode. The current n-doped Si substrate (bottom electrode) with limited electrical conductivity can introduce energy losses, which could be solved by using a conductive AZO or Au layer instead [16]. In conclusion, the conformal deposition of a parylene-C layer with controlled thickness significantly enhanced the

performance of a ZnO NW-based PNG, opening pathways for improved fabrication of flexible and rigid PNGs.

4. Conclusion

The performance optimization of ZnO NW-based PNGs through the control of the parylene-C top layer thickness was investigated. FESEM images have confirmed the fabrication of four different PNGs with parylene-C top layer thicknesses of 1.11, 1.98, 2.93, and 3.34 μm . The parylene-C successfully impregnates the ZnO NW arrays, but its density distribution over the NW arrays appears non-homogeneous, as FESEM-EDS maps have revealed. Raman spectroscopy has identified the phonon modes of parylene-C, mainly associated with carbon-related bonds, and suggested that the parylene-C layer does not induce any mechanical stress in ZnO NWs. This indicates that parylene-C coating layer is unlikely to affect the spontaneous polarization of the ZnO NWs. Moreover, an increase in the internal impedance of the PNGs has been observed with thicker parylene-C top layers, with values exceeding 49.5 M Ω . Piezoelectric measurements have demonstrated that the PNG with a 1.98 μm -thick parylene-C top layer produces the highest output voltage and instantaneous power density, measuring 267.4 mV (over a load resistance of 122 M Ω , being the maximum value tested) and 1.8 $\mu\text{W}/\text{cm}^3$ (over a load resistance of 10 M Ω , being the optimal value), respectively. These findings indicate that a parylene-C top layer thickness of about 2 μm is an optimal balance between mechanical energy transfer and electrical energy conversion of a vertically-integrated ZnO NW-based PNG.

Table 1

Output voltage and power density values generated by PNGs based on PMMA, PDMS, and parylene-C matrix along with vertically integrated ZnO NWs grown by the CBD / hydrothermal method.

Substrate	ZnO NW features Length (L - μm) Diameter (ϕ - nm) Density (D - $\text{NW } \mu\text{m}^{-2}$) Aspect ratio ($AR = \phi/L$)	Polymer	Mechanical stress	External Load (M Ω)	Output voltage	Power density	REF
PET ⁽¹⁾ / Ti / Ni / SiO ₂ / Ti / Ni	L : 2 ϕ : 200	PMMA (Unknown thickness)	Bending force at 10 Hz	1	54 mV _{pp}		[26]
PET / Ti / Ni / SiO ₂ / Ti / Ni	ϕ : 200	PMMA (Unknown thickness)	Deflection of 2 mm at 100 Hz	1	60 mV _{pp}	0.144 mW/cm ²	[47]
Si / Ti / Au	L : 1.1 ϕ : 45 AR : 25	PMMA (Unknown thickness)	Compression of 6 N at 9 Hz	4		0.9 mW/cm ³	[48]
Si (p-type) / ZnO	Not specified	PMMA (Unknown thickness)	Compression of 5 N	1		85 $\mu\text{W}/\text{cm}^3$	[21]
PEN ⁽²⁾ / Ti / Au	L : 0.97 ± 0.34 ϕ : 115 ± 64	PDMS (7 μm over the NWs)	Deflection of 3–4 mm at 20 Hz	1		288 nW/cm ³	[14]
Si / Ti / Au	L : 0.97 ± 0.34 ϕ : 115 ± 64 D : 74.5 ± 6.5	PDMS (7 μm over the NWs)	Compression at 10 Hz	1		4 $\mu\text{W}/\text{cm}^3$	[49]
Si / Ti / Au	Not specified	PDMS (10 μm over the NWs)	Compression of 6 N at 10 Hz	1	4.2 mV _{pp}		[50]
PDMS ⁽³⁾ / Ti / Pt / ZnO	Not specified	Parylene-C (600 nm)	Compression of 13 N at 5 Hz	8		4 mW/cm ³	[25]
Quartz / AZO	L : 0.48 ± 0.08 ϕ : 140 ± 60 D : 52.9 ± 0.5	Parylene-C (some hundreds of nm)	Compression of 3 N at 5 Hz	0.177	36 mV	2.5 mW/cm ² (23.1 $\mu\text{W}/\text{cm}^3$)	[16]
Si / Ti / Au / ZnO	L : 0.57 ± 0.18 ϕ : 0.07 ± 0.03 D : 35.4 ± 0.2	Parylene-C (some hundreds of nm)	Compression of 3 N at 5 Hz	0.562	272 mV	14.2 nW/cm ² (1.2 mW/cm ³)	[16]
Si / Ti / Au	L : 1.2	Parylene-C (300 nm over the NWs)	Compression of 5 N at 3 Hz	1	950 mV	1 $\mu\text{W}/\text{cm}^3$	[51]
Si (n-type) / ZnO	L : 5.5 ± 0.4 ϕ : 166 ± 40 D : 43.3 ± 8.2 AR : 33.1 ± 8.3	Parylene-C (1.98 μm over the NWs)	Compression of 1 N at 0.2 Hz	10	119.2 mV	1.36 nW/cm ² or 1.8 $\mu\text{W}/\text{cm}^3$	This work (PNG-B)

¹ PET: Poly(ethylene terephthalate).

² PEN: Poly(ethylene naphthalate).

³ PDMS: Poly(dimethylsiloxane).

The values of 23.1 $\mu\text{W}/\text{cm}^3$ and 1.2 mW/cm³ were estimated using the information provided in the referred paper.

CRediT authorship contribution statement

Manuel Manrique: Writing – review & editing, Writing – original draft, Visualization, Investigation, Formal analysis, Data curation, Conceptualization. **Vincent Consonni:** Writing – review & editing, Writing – original draft, Validation, Supervision, Resources, Project administration, Funding acquisition, Conceptualization. **Gustavo Ardila:** Writing – review & editing, Investigation, Formal analysis, Conceptualization. **Aymen Ghouma:** Writing – review & editing, Investigation, Formal analysis. **Gwenaël Le Rhun:** Writing – review & editing, Writing – original draft, Validation, Supervision, Resources, Funding acquisition, Conceptualization. **Bassem Salem:** Writing – review & editing, Writing – original draft, Validation, Supervision, Resources, Project administration, Funding acquisition, Conceptualization.

Declaration of competing interest

The authors declare that they have no known competing financial interests or personal relationships that could have appeared to influence the work reported in this paper.

Acknowledgments

This work was partially supported by LabEx MINOS under the contract ANR-10-LABX-55-01 and the French RENATECH network through the PTA technological platforms. M.M. held a doctoral fellowship from LabEx MINOS. V.C. also acknowledges the financial support from the French National Research Agency through the project IMINEN (ANR-22-CE09-0032). This research has also benefited from some of the characterization equipments of the Grenoble INP-CMTC platform.

References

- A. Zanella, N. Bui, A. Castellani, L. Vangelista, M. Zorzi, Internet of things for smart cities, *IEEE Internet Things J.* 1 (1) (2014) 22–32, <https://doi.org/10.1109/JIOT.2014.2306328>.
- I. Izadgoshasb, Piezoelectric energy harvesting towards self-powered internet of things (IoT) sensors in smart cities, *Sensors* 21 (24) (2021) 8332, <https://doi.org/10.3390/s21248332>.
- X. Cao, Y. Xiong, J. Sun, X. Zhu, Q. Sun, Z.L. Wang, Piezoelectric nanogenerators derived self-powered sensors for multifunctional applications and artificial intelligence, *Adv. Funct. Mater.* 31 (33) (2021) 1–31, <https://doi.org/10.1002/adfm.202102983>.
- K.K. Das, B. Basu, P. Maiti, A.K. Dubey, Piezoelectric nanogenerators for self-powered wearable and implantable bioelectronic devices, *Acta Biomater.* 171 (2023) 85–113, <https://doi.org/10.1016/j.actbio.2023.08.057>.
- B. Zaarour, L. Zhu, C. Huang, X. Jin, H. Alghafari, J. Fang, T. Lin, A review on piezoelectric fibers and nanowires for energy harvesting, *J. Ind. Text.* 51 (2) (2021) 297–340, <https://doi.org/10.1177/1528083719870197>.
- Z.L. Wang, J. Song, Piezoelectric nanogenerators based on zinc oxide nanowire arrays, *Science* 312 (5771) (2006) 242–246, <https://doi.org/10.1126/science.1124005>.
- S. Lee, R. Hinchet, Y. Lee, Y. Yang, Z. Lin, G. Ardila, L. Montès, M. Mouis, Z. L. Wang, Ultrathin nanogenerators as self-powered/active skin sensors for tracking eye ball motion, *Adv. Funct. Mater.* 24 (8) (2014) 1163–1168, <https://doi.org/10.1002/adfm.201301971>.
- R. Hinchet, S. Lee, G. Ardila, L. Montès, M. Mouis, Z.L. Wang, Performance optimization of vertical nanowire-based piezoelectric nanogenerators, *Adv. Funct. Mater.* 24 (7) (2014) 971–977, <https://doi.org/10.1002/adfm.201302157>.
- R. Hinchet, S. Lee, G. Ardila, L. Montès, M. Mouis, Z.L. Wang, Design and guideline rules for the performance improvement of vertically integrated nanogenerator, *Proc. PowerMEMS 7* (7) (2013) 4.
- G. Zhu, A.C. Wang, Y. Liu, Y. Zhou, Z.L. Wang, Functional electrical stimulation by nanogenerator with 58 V output voltage, *Nano Lett.* 12 (6) (2012) 3086–3090, <https://doi.org/10.1021/nl300972f>.
- D. Yang, Y. Qiu, Q. Jiang, Z. Guo, W. Song, J. Xu, Y. Zong, Q. Feng, X. Sun, Patterned growth of ZnO nanowires on flexible substrates for enhanced performance of flexible piezoelectric nanogenerators, *Appl. Phys. Lett.* 110 (6) (2017), <https://doi.org/10.1063/1.4975477>.
- S. Kannan, M. Parmar, R. Tao, G. Ardila, M. Mouis, Optimization of dielectric matrix for ZnO nanowire based nanogenerators, *J. Phys. Conf. Ser.* 773 (1) (2016), <https://doi.org/10.1088/1742-6596/773/1/012071>.
- X. Zhang, J. Villafuerte, V. Consonni, J.-F. Capsal, P.-J. Cottinet, L. Petit, M.-Q. Le, Characterizing and optimizing piezoelectric response of ZnO nanowire/PMMA composite-based sensor, *Nanomaterials* 11 (7) (2021) 1712, <https://doi.org/10.3390/nano11071712>.
- C. Opoku, A.S. Dahiya, C. Oshman, F. Cayrel, G. Poulin-Vittrant, D. Alquier, N. Camara, Fabrication of ZnO nanowire based piezoelectric generators and related structures, *Phys. Procedia* 70 (2015) 858–862, <https://doi.org/10.1016/j.phpro.2015.08.176>.
- A.S. Dahiya, F. Morini, S. Boubenia, K. Nadaud, D. Alquier, G. Poulin-Vittrant, Organic/inorganic hybrid stretchable piezoelectric nanogenerators for self-powered wearable electronics, *Adv. Mater. Technol.* 3 (2) (2018) 1–11, <https://doi.org/10.1002/admt.201700249>.
- C. Justeau, T.S. Tlemcani, G. Poulin-Vittrant, K. Nadaud, D. Alquier, A comparative study on the effects of Au, ZnO and AZO seed layers on the performance of ZnO nanowire-based piezoelectric nanogenerators, *Materials (Basel)* 12 (16) (2019), <https://doi.org/10.3390/ma12162511>.
- C. Ou, P.E. Sanchez-Jimenez, A. Datta, F.L. Boughey, R.A. Whiter, S.L. Sahonta, S. Kar-Narayan, Template-assisted hydrothermal growth of aligned zinc oxide nanowires for piezoelectric energy harvesting applications, *ACS Appl. Mater. Interfaces* 8 (22) (2016) 13678–13683, <https://doi.org/10.1021/acsami.6b04041>.
- F.E.B. Anang, A.D. Refino, G. Harm, D. Li, J. Xu, M. Cain, U. Brand, Z. Li, M. Görke, G. Garnweiner, E. Peiner, Thermo-convective solution growth of vertically aligned zinc oxide nanowire arrays for piezoelectric energy harvesting, *Micromachines* 15 (10) (2024) 1179, <https://doi.org/10.3390/mi15101179>.
- F.E.B. Anang, X. Wei, J. Xu, M. Cain, Z. Li, U. Brand, E. Peiner, Area-selective growth of zinc oxide nanowire arrays for piezoelectric energy harvesting, *Micromachines* 15 (2) (2024) 261, <https://doi.org/10.3390/mi15020261>.
- N. Doumit, G. Poulin-Vittrant, Effect of the dielectric and mechanical properties of the polymer matrix on ZnO-nanowire-based composite nanogenerators performance, *Adv. Theory Simul.* 3 (9) (2020) 1–9, <https://doi.org/10.1002/adts.202000128>.
- R. Tao, M. Parmar, G. Ardila, P. Oliveira, D. Marques, L. Montès, M. Mouis, Performance of ZnO based piezo-generators under controlled compression, *Semicond. Sci. Technol.* 32 (6) (2017), <https://doi.org/10.1088/1361-6641/aa691f>.
- L. Lin, Y. Hu, C. Xu, Y. Zhang, R. Zhang, X. Wen, Lin Wang, Z. Transparent flexible nanogenerator as self-powered sensor for transportation monitoring, *Nano Energy* 2 (1) (2013) 75–81, <https://doi.org/10.1016/j.nanoen.2012.07.019>.
- C. Hassler, R.P. von Metzzen, P. Ruther, T. Stieglitz, Characterization of parylene C as an encapsulation material for implanted neural prostheses, *J. Biomed. Mater. Res. Part B Appl. Biomater.* 93B (1) (2010) 266–274, <https://doi.org/10.1002/jbm.b.31584>.
- A. Kahouli, A. Sylvestre, L. Ortega, F. Jomni, B. Yangui, M. Maillard, B. Berge, J. C. Robert, J. Legrand, Structural and dielectric study of parylene C thin films, *Appl. Phys. Lett.* 94 (15) (2009), <https://doi.org/10.1063/1.3114404>.
- A.S. Dahiya, F. Morini, S. Boubenia, C. Justeau, K. Nadaud, K.P. Rajeev, D. Alquier, G. Poulin-Vittrant, Zinc oxide nanowire-parylene nanocomposite based stretchable piezoelectric nanogenerators for self-powered wearable electronics, *J. Phys. Conf. Ser.* 1052 (1) (2018), <https://doi.org/10.1088/1742-6596/1052/1/012028>.
- G. Poulin-Vittrant, C. Oshman, C. Opoku, A.S. Dahiya, N. Camara, D. Alquier, L.-P. T.H. Hue, M. Lethieq, Fabrication and characterization of ZnO nanowire-based piezoelectric nanogenerators for low frequency mechanical energy harvesting, *Phys. Procedia* 70 (2015) 909–913, <https://doi.org/10.1016/j.phpro.2015.08.188>.
- W.F. Gorham, A new, general synthetic method for the preparation of linear poly-p-xylylenes, *J. Polym. Sci. Part A-1 Polym. Chem.* 4 (12) (1966) 3027–3039, <https://doi.org/10.1002/pol.1966.150041209>.
- S. Guillemin, V. Consonni, E. Appert, E. Puyoo, L. Rapenne, H. Roussel, Critical nucleation effects on the structural relationship between ZnO seed layer and nanowires, *J. Phys. Chem. C* 116 (47) (2012) 25106–25111, <https://doi.org/10.1021/jp308643w>.
- J. Villafuerte, E. Sarigiannidou, F. Donatini, J. Kioseoglou, O. Chaix-Pluchery, J. Pernot, V. Consonni, Modulating the growth of chemically deposited ZnO nanowires and the formation of nitrogen- and hydrogen-related defects using PH adjustment, *Nanoscale Adv.* 4 (7) (2022) 1793–1807, <https://doi.org/10.1039/d1na00785h>.
- R. Cuscó, E. Alarcón-Lladó, J. Ibáñez, L. Artús, J. Jiménez, B. Wang, M.J. Callahan, Temperature dependence of Raman scattering in ZnO, *Phys. Rev. B* 75 (16) (2007) 165202, <https://doi.org/10.1103/PhysRevB.75.165202>.
- M.S. Mathur, N.A. Weir, Laser Raman and infrared spectrum of poly-p-xylylene, *J. Mol. Struct.* 15 (3) (1973) 459–463, [https://doi.org/10.1016/0022-2860\(73\)80016-X](https://doi.org/10.1016/0022-2860(73)80016-X).
- M.H. Yang, S.W. Jeong, S.J. Chang, K.H. Kim, M. Jang, C.H. Kim, N.H. Bae, G. S. Sim, T. Kang, S.J. Lee, B.G. Choi, K.G. Lee, Flexible and disposable sensing platforms based on newspaper, *ACS Appl. Mater. Interfaces* 8 (51) (2016) 34978–34984, <https://doi.org/10.1021/acsami.6b10298>.
- R. Parize, J. Garnier, O. Chaix-Pluchery, C. Verrier, E. Appert, V. Consonni, Effects of hexamethylenetetramine on the nucleation and radial growth of ZnO nanowires by chemical bath deposition, *J. Phys. Chem. C* 120 (9) (2016) 5242–5250, <https://doi.org/10.1021/acs.jpcc.6b00479>.
- J. Villafuerte, O. Chaix-Pluchery, J. Kioseoglou, F. Donatini, E. Sarigiannidou, J. Pernot, V. Consonni, Engineering nitrogen- and hydrogen-related defects in ZnO nanowires using thermal annealing, *Phys. Rev. Mater.* 5 (5) (2021) 1–15, <https://doi.org/10.1103/PhysRevMaterials.5.056001>.
- J.L. Lyons, J.B. Varley, D. Steiauf, A. Janotti, C.G. Van De Walle, First-principles characterization of native-defect-related optical transitions in ZnO, *J. Appl. Phys.* 122 (3) (2017), <https://doi.org/10.1063/1.4992128>.
- F. Herklotz, A. Hupfer, K.M. Johansen, B.G. Svensson, S.G. Koch, E.V. Lavrov, Infrared absorption on a complex comprising three equivalent hydrogen atoms in ZnO, *Phys. Rev. B - Condens. Matter Mater. Phys.* 92 (15) (2015) 1–10, <https://doi.org/10.1103/PhysRevB.92.155203>.

- [37] E.V. Lavrov, J. Weber, F. Börrnert, C.G. Van de Walle, R. Helbig, Hydrogen-related defects in ZnO studied by infrared absorption spectroscopy, *Phys. Rev. B - Condens. Matter Mater. Phys.* 66 (16) (2002) 1–7, <https://doi.org/10.1103/PhysRevB.66.165205>.
- [38] E. Lavrov, Infrared absorption spectroscopy of hydrogen-related defects in ZnO, *Phys. B Condens. Matter* 340–342 (2003) 195–200, <https://doi.org/10.1016/j.physb.2003.09.032>.
- [39] E.V. Lavrov, F. Börrnert, J. Weber, Dominant hydrogen-oxygen complex in hydrothermally grown ZnO, *Phys. Rev. B* 71 (3) (2005) 035205, <https://doi.org/10.1103/PhysRevB.71.035205>.
- [40] K.M. Balss, G. Llanos, G. Papandreou, C.A. Maryanoff, Quantitative spatial distribution of sirolimus and polymers in drug-eluting stents using confocal Raman microscopy, *J. Biomed. Mater. Res. - Part A* 85 (1) (2008) 258–270, <https://doi.org/10.1002/jbm.a.31535>.
- [41] F. Decremps, J. Pellicer-Porres, A.M. Saitta, J.-C. Chervin, A. Polian, High-pressure Raman spectroscopy study of wurtzite ZnO, *Phys. Rev. B* 65 (9) (2002) 092101, <https://doi.org/10.1103/PhysRevB.65.092101>.
- [42] F. Bernardini, V. Fiorentini, D. Vanderbilt, Spontaneous polarization and piezoelectric constants of III–V nitrides, *Phys. Rev. B* 56 (16) (1997) R10024–R10027, <https://doi.org/10.1103/PhysRevB.56.R10024>.
- [43] C. Noguera, F. Finocchi, J. Goniakowski, First principles studies of complex oxide surfaces and interfaces, *J. Phys. Condens. Matter* 16 (26) (2004) S2509–S2537, <https://doi.org/10.1088/0953-8984/16/26/025>.
- [44] A. Šutka, P.C. Sherrell, N.A. Shepelin, L. Lapčinskis, K. Málnieks, A.V. Ellis, Measuring piezoelectric output—fact or friction? *Adv. Mater.* 32 (32) (2020) 1–9, <https://doi.org/10.1002/adma.202002979>.
- [45] K. Nadaud, G. Poulin-Vittrant, D. Alquier, Effect of the excitation waveform on the average power and peak power delivered by a piezoelectric generator, *Mech. Syst. Signal Process.* 133 (2019) 106278, <https://doi.org/10.1016/j.ymssp.2019.106278>.
- [46] K. Nadaud, F. Morini, A.S. Dahiya, C. Justeau, S. Boubenia, K.P. Rajeev, D. Alquier, G. Poulin-Vittrant, Double buffer circuit for the characterization of piezoelectric nanogenerators based on ZnO nanowires, *Appl. Phys. Lett.* 112 (6) (2018) 1–6, <https://doi.org/10.1063/1.5018145>.
- [47] C. Oshman, J. Chauvin, C. Opoku, A.S. Dahiya, D. Alquier, M. Lethiecq, N. Camara, G. Poulin-Vittrant, Energy harvesting using galvanically synthesized piezoelectric ZnO nanorods on flexible polymer film. Volume 6B: Energy, American Society of Mechanical Engineers, 2015, pp. 2015–2018, <https://doi.org/10.1115/IMECE2015-52259>.
- [48] L. Serairi, Y. Leprince-Wang, ZnO nanowire-based piezoelectric nanogenerator device performance tests, *Crystals* 12 (8) (2022) 1023, <https://doi.org/10.3390/cryst12081023>.
- [49] C. Opoku, A.S. Dahiya, F. Cayrel, G. Poulin-Vittrant, D. Alquier, N. Camara, Fabrication of field-effect transistors and functional nanogenerators using hydrothermally grown ZnO nanowires, *RSC Adv.* 5 (86) (2015) 69925–69931, <https://doi.org/10.1039/c5ra11450k>.
- [50] C. Oshman, C. Opoku, A.S. Dahiya, D. Alquier, N. Camara, G. Poulin-Vittrant, Measurement of spurious voltages in ZnO piezoelectric nanogenerators, *J. Microelectromechanical Syst.* 25 (3) (2016) 533–541, <https://doi.org/10.1109/JMEMS.2016.2538206>.
- [51] F. Morini, A.S. Dahiya, S. Boubenia, C. Opoku, G. Poulin-Vittrant, F. Cayrel, D. Alquier, Fabrication and functional characterization of ZnO nanowire based piezoelectric nanogenerators. 13th Expert Evaluation and Control of Compound Semiconductor Materials and Technologies (EXMATEC), Aveiro, Portugal, Jun 2016. (hal-03591413).

Further reading

- [52] R. Tao, M. Parmar, G. Ardila, P. Oliveira, D. Marques, L. Montès, M. Mouis, Performance of ZnO based piezo-generators under controlled compression, *Semicond. Sci. Technol.* 32 (6) (2017), <https://doi.org/10.1088/1361-6641/aa691f>.